www.czasopisma.pan.pl PAN POLSKA AKADEMIA NAUK www.journals.pan.pl

Arch. Metall. Mater. **64** (2019), 2, 565-569

DOI: 10.24425/amm.2019.127579

JUN YOUNG SUH*, YO-SEUNG SONG*, SI YOUNG CHANG*#

SPARK PLASMA SINTERING OF Mn-Zn FERRITE POWDERS BY HIGH ENERGY BALL MILLING

The Mn-Zn ferrite powders prepared by high energy ball milling were heat-treated, subsequently compacted and sintered by spark plasma sintering (SPS). Based on the observation of microstructure, the characteristics of samples after SPS were investigated and compared with ones after conventional sintering. The size of initial powders was approximately 650 nm and decreased to 230 nm after milling at 300 rpm for 3 h. After heat treatment at 973K for 1h, the milled powders became larger to approximately 550 nm in size again and the peaks of Mn_2O_3 disappeared in XRD patterns. In the samples after SPS, the Fe_2O_3 and $MnZnFe_2O_4$ phases decomposed at the higher temperatures than 1173K and 1373K, respectively, while only $MnZnFe_2O_4$ phase was detected in the samples conventionally sintered at 1273~1673K. As the sintering temperature increased, the relative density after SPS increased more quickly than that after conventional sintering. In particular, it reached approximately 99% after SPS at 1473K.

Keywords: High energy ball milling, Nano-sized particles, SPS, Conventional sintering, Density

1. Introduction

Recently, the wireless power transfer technology that supplies the power in homes and commercial appliances without electric wire has received great attention. The electromagnetic induction, magnetic resonance and electromagnetic radiation are general methods for wireless power transfer. Among them, the electromagnetic induction has been applied to portable electronics. Mn-Zn ferrite core is most suitable electromagnetic materials for wireless power transfer because of high initial permeability, high saturation magnetization, low eddy current and coercivity [1].

Mn-Zn ferrite core could be produced by powder metallurgy processing. In general, the magnetic performance of Mn-Zn ferrite core depends on the characteristics of powders [2], and the soft magnetic properties are improved in ultra-fined or nanocrystalline alloys [3]. Among powder metallurgy processing, high energy ball milling is an effective method currently used to obtain amorphous phase or nanocrystalline structure in inorganic materials synthesis [4-6]. On the other hand, the nano-sized powders obtained by high energy ball milling are rapidly ripened because they are exposed to high temperature for a long time during subsequent conventional sintering.

Recently, the spark plasma sintering (SPS) method has received the spotlight for rapid heating rate, short holding time, low temperature, high sintering density and easy manipulation compared to other conventional sintering methods [7,8]. In the SPS, initial powder materials are sintered by joule heat occurring from spark plasma generated in the gap between powder materials under pressure in uniaxial direction. The SPS has been applied for new materials, such as fine ceramics [9,10], nano phase materials [11], hard alloy tool materials [12], magnetic materials [13] and ferrous materials[14], etc.

In this study, therefore, Mn-Zn ferrite powders produced by high energy ball milling were heat-treated and subsequently sintered by the SPS. Additionally, the microstructural characteristics of samples sintered by the SPS were investigated and compared to those of the conventionally sintered samples.

2. Experimental

The initial ferrite powders composed of Fe_2O_3, Mn_2O_3 and $MnZnFe_2O_4$ oxides were charged with stainless ball into jars in high energy ball milling equipment. The ball milling was conducted with the ball to powder weight ratio of 20:1 and the milling rate of 300 rpm for 3 h under argon atmosphere. The milled powders were collected in the glove box filled with argon gas, and subsequently heat-treated at 973K for 1h under argon atmosphere for the pre-synthesis of $MnZnFe_2O_4$ phase. The heat-treated powders were uniaxially compacted under a pressure of 90 MPa for 3 min. Some of them were conventionally sintered at 1273~1673K for 3 h under argon atmosphere and some of them were subjected to spark plasma sintering with the applied pressure of 60 MPa at 1173~1473K for 5min in a vacuum.

The microstructural characteristics of the powders and the sintered samples were observed by using a scanning electron microscope (SEM) and a transmission electron microscope

* KOREA AEROSPACE UNIVERSITY, DEPARTMENT OF MATERIALS ENGINEERING, GOYANG 10540, KOREA

Corresponding author: sychang@kau.ac.kr

(TEM). The powder size and shape were investigated by an image analysis. In particular, the shape was evaluated with a shape factor (= $4\pi A/P^2$, where A is area and P is perimeter of powder). The mean particle size was calculated by Debye-Scherrer's equation using the half-value width of peaks [15]. The identification of phases was carried out by an X-ray diffractometer (XRD). The relative density of the sintered samples was obtained by Archimedes method.

3. Results and discussion

The typical SEM photographs of initial, as milled and as heat-treated ferrite powders are shown in Fig. 1(a), (b) and (c), respectively. The initial ferrite powders are irregular in shape and there is no marked change of shape after milling and heat treatment. After milling, the initial powders become obviously smaller. However, the milled powders have been growing again after heat treatment. The mean powder size, shape factor and size distribution obtained from Fig. 1 are quantitatively plotted in Fig. 2. The mean size of approximately 650 nm in the initial powders is reduced to approximately 230 nm after milling at 300 rpm for 3 h. After heat-treatment at 973K for 1h, however, it increases to approximately 550 nm. The shape factor of initial powders is approximately 0.7, and it is almost unchanged even after milling and heat treatment. The size distribution of initial powders is in between 200 and 2000 nm and greatly moves to 60~700 nm after milling. The heat-treated powders show 100~2000 nm in size distribution. The highest number peaks of powders well correspond to the mean size of powders.

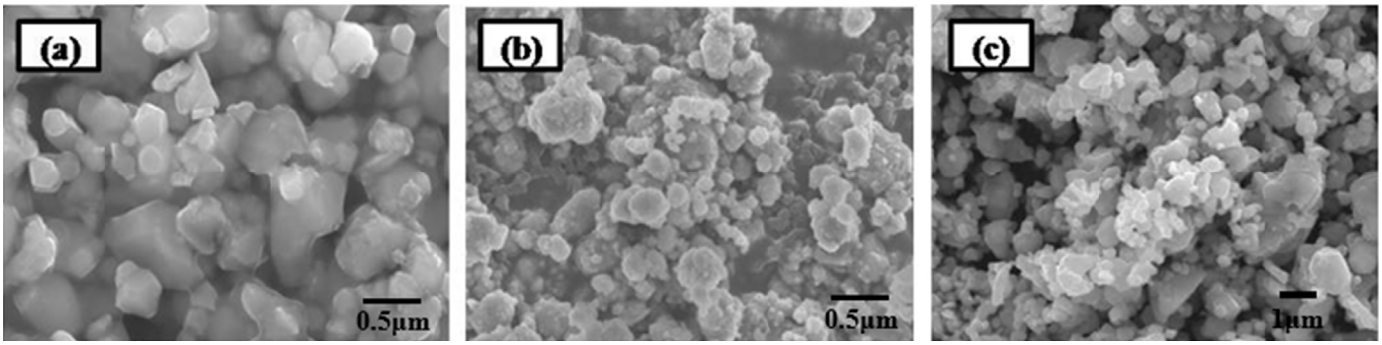

Fig. 1. SEM images showing ferrite powders ; (a) initial state, (b) after milling at 300 rpm for 3 h and (c) after heat treatment at 973K for 1 h

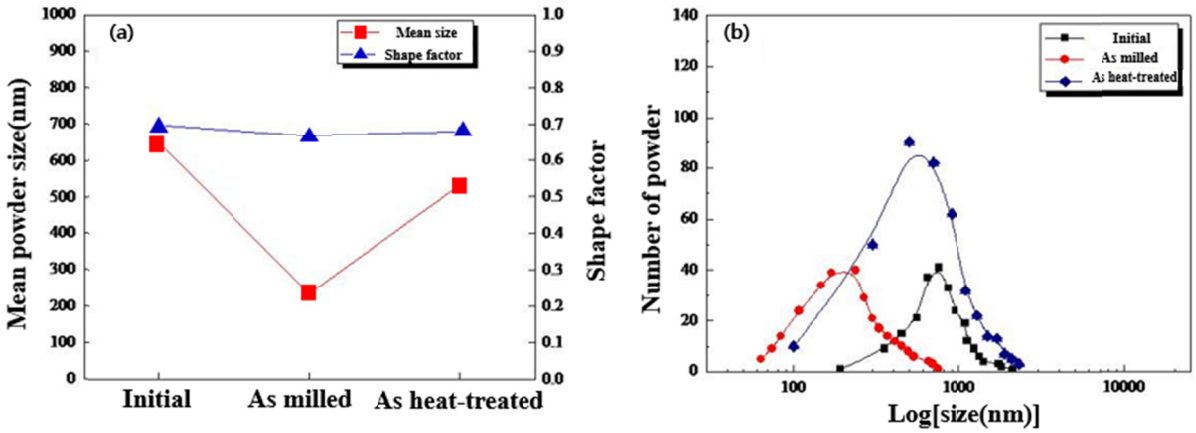

Fig. 2. (a) Mean powder size, shape factor and (b) size distribution of the initial, as milled and as heat-treated ferrite powders

Figure 3 shows XRD patterns of the initial, as milled and as heat-treated ferrite powders. The peaks of the Fe_2O_3, Mn_2O_3 and $MnZnFe_2O_4$ phases are observed in the initial powders. The peaks are unchanged after milling, while, after heat treatment, the peaks of Mn_2O_3 phase disappear and the $MnZnFe_2O_4$ phase is obviously detected with the unreacted Fe_2O_3 phase.

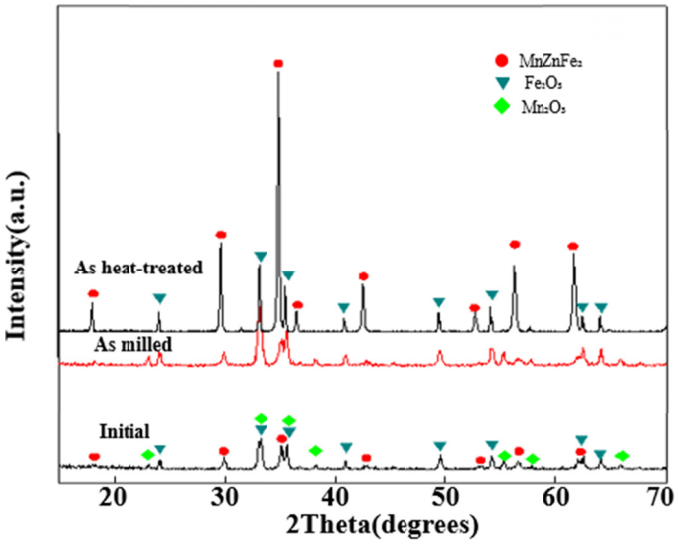

Fig. 3. XRD patterns of the initial, as milled and as heat-treated ferrite powders

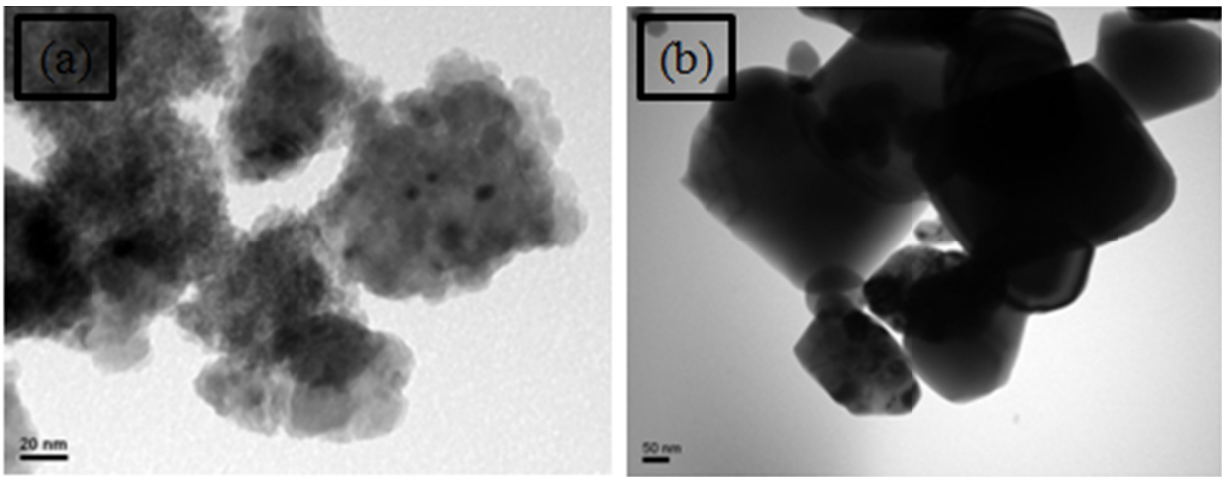

Fig. 4. TEM images of (a) as milled and (b) as heat-treated ferrite powders

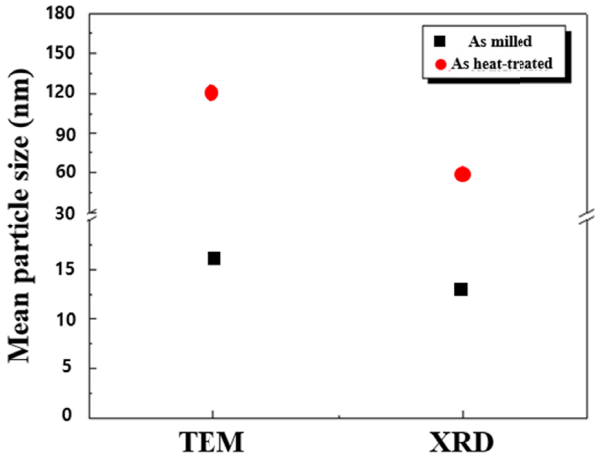

Fig. 5. Mean particle sizes of as milled and as heat-treated ferrite powders

Figure 4 shows TEM photographs of as milled and as heat-treated ferrite powders. The milled ferrite powders with the mean size of approximately 230 nm as shown in Fig. 1 and 2 are composed of nano-sized particles (≒15 nm). After heat treatment, the growth of particles occurs, resulting in the increase of mean size that becomes approximately 120 nm. The particle size measured from Fig. 4 is quantitatively plotted in Fig. 5, together with that obtained from Fig. 3. Based on the calculation by Debye-Scherrer's equation, the mean particle sizes of as milled and as heat-treated powders are approximately 12 nm and 60 nm, respectively, which relatively well corresponds to ones measured from TEM images.

The microstructures of the conventionally sintered samples with increasing the sintering temperature are shown in Fig. 6, along with a photograph of the compacted sample with a green density of approximately 53% and a disc shape of 8 mm in diameter and 4.43 mm in thickness used for SPS and conventional sintering. As the sintering temperature increases, the microstructure becomes much denser. At 1273K, the agglomerated powders and many pores are observed, while the densification obviously occurs at more than 1373K.

Figure 7 shows appearances and SEM photographs of as heat-treated powders sintered by SPS at 1173~1473K for 5 min. The compacted samples with 8mm in diameter and 4.43 mm in thickness are shrunk by SPS, and the shrinkage becomes larger with increasing the sintering temperature. However, there are no observable cracks in the appearance of sintered body. On the other hand, after SPS at 1173K, the agglomerated powders and many voids were observed, indicating that sufficient substance migration including diffusion had not occurred during sintering [16]. The sample sintered at 1273K shows obviously necks between grown grains, but there still exist open pores. However, the grains become much larger and the pores are obviously reduced

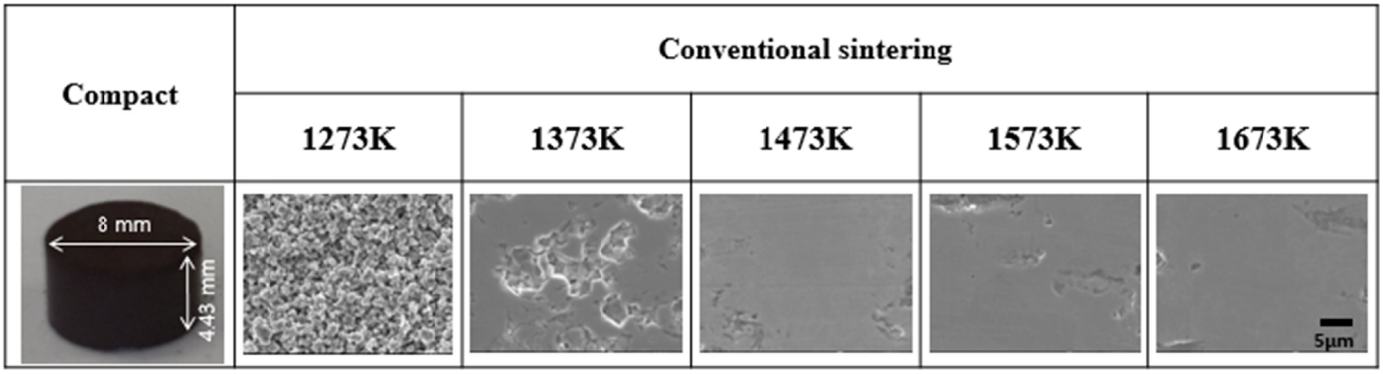

Fig. 6. SEM images showing microstructures of the samples after conventional sintering at various temperatures

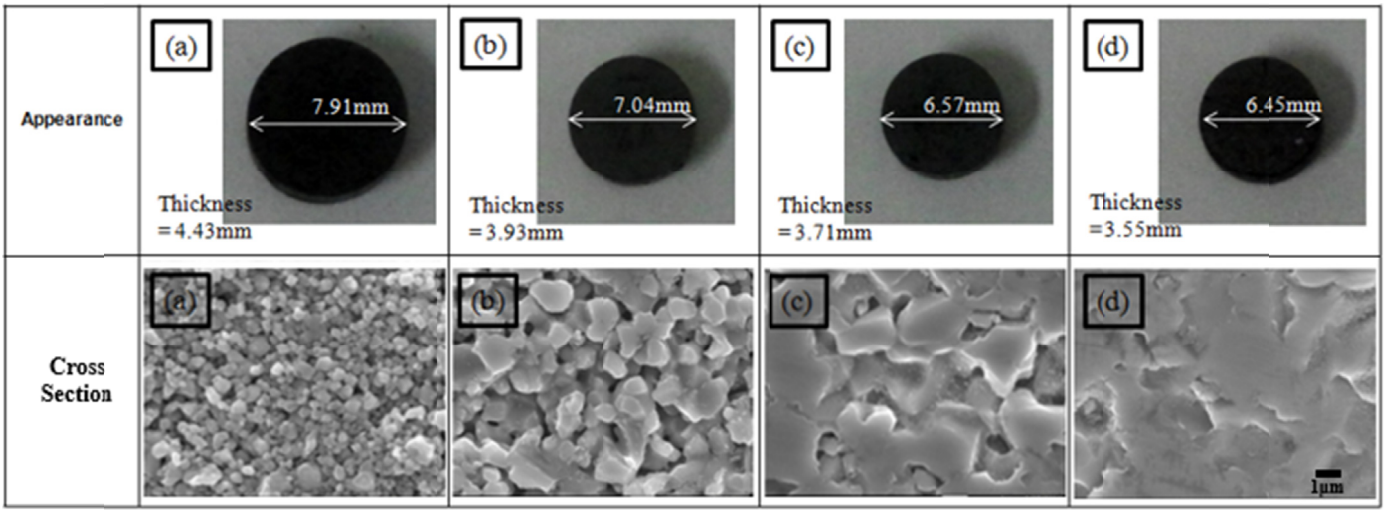

Fig. 7. Appearances and SEM images of the samples after SPS at (a) 1173K, (b) 1273K, (c) 1373K and (e) 1473K

at more than 1373K. In particular, the sample sintered at 1473K is fully densified.

Figure 8 shows the XRD patterns of the sintered samples. After conventional sintering at 1273~1673K, there are no peaks of Fe_2O_3 phase, while, in case of SPS, the Fe_2O_3 phase is detected at 1173K and its peaks completely disappear at 1273K. This indicates that the Fe_2O_3 phase decomposed at higher temperatures than 1173K. On the other hand, the $MnZnFe_2O_4$ phase is detected after conventional sintering at all temperatures. However, during SPS, the $MnZnFe_2O_4$ phase begins to decompose at 1373K and completely disappears at 1473K, and the formation of FeO and MnO phases concurrently occurs, which is generally considered

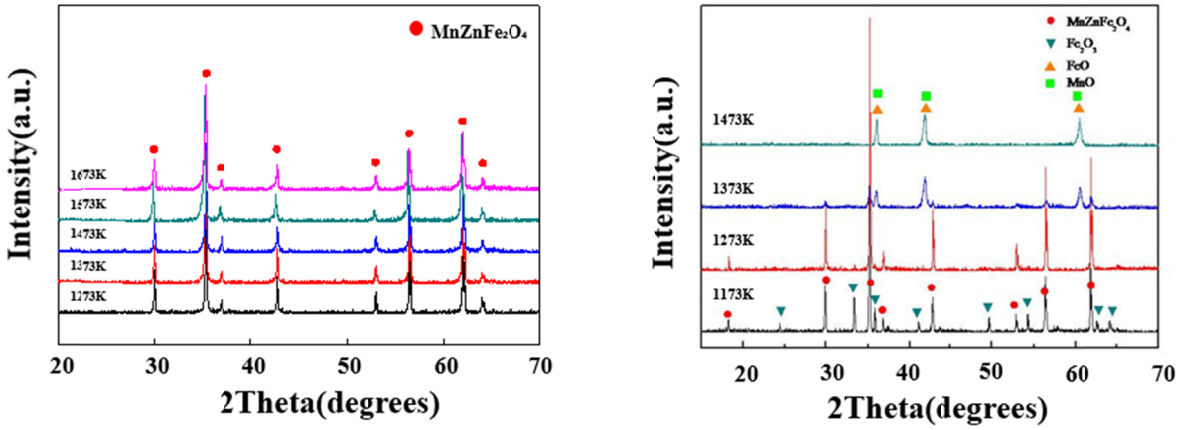

Fig. 8. XRD patterns of the samples after (a) conventional sintering and (b) SPS at various temperatures

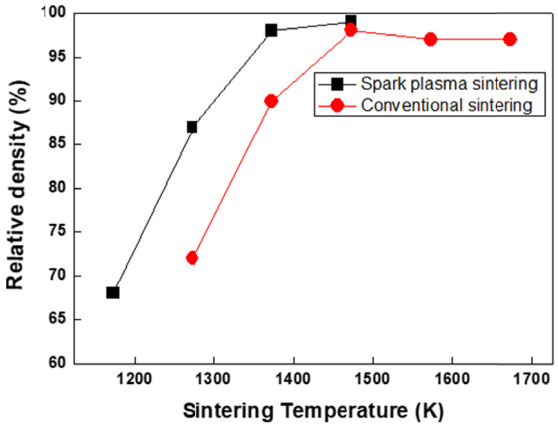

Fig. 9. Relative density of the sintered samples with increasing the sintering temperature

to be due to the effective transfer of joule heat occurring from spark plasma.

The change of relative density in the samples sintered by SPS with increasing the sintering temperature is shown in Fig. 9, in comparison to that in the conventionally sintered samples. As the sintering temperature increases, the relative density increases. However, the SPS causes much rapid increase of relative density, resulting in much higher relative density than the conventional sintering at same temperature. This is also considered to stem from the effective transfer of joule heat occurring from spark plasma during short heating and holding in SPS [7,8]. In particular, the sample sintered by SPS at 1473K showing dense microstructure has the highest relative density of approximately 99%.

4. Conclusions

The milled ferrite powders at 300 rpm for 3 h had the size of approximately 230 nm, which consisted of nano-sized particles of approximately 15 nm in size. The powders consisted of the Mn_2O_3, Fe_2O_3 and $MnZnFe_2O_4$ phases. After heat treatment at 973K for 1h, the mean size of agglomerated powders increased from 230 nm to 550 nm and the particles became larger to approximately 120 nm. In addition, the Mn_2O_3 phase decomposed. The Fe_2O_3 and $MnZnFe_2O_4$ phases completely disappeared after SPS at temperatures of 1273K and 1473K, respectively, while the FeO and MnO phases formed at higher temperatures than 1273K. After conventional sintering at 1273~1673K, however, the only $MnZnFe_2O_4$ phase was detected. As the sintering temperature increased, the relative density after SPS and conventional sintering increased. In addition, the SPS caused much higher relative density than the convention sintering, and the sample sintered by SPS at 1473K showed the densest microstructure with the relative density of approximately 99%.

REFERENCES

[1] P. Hu, H. Yang, D. Pan, H. Wang, J. Tian, S. Zhang, X. Wang, A.A. Volinsky, J. Magn. Magn. Mater. **322**, 173-177 (2010).

[2] S.K. Pradhan, S. Bid, M. Gateshki, V. Petkov, J. Mater. Chem. Phys. **93**, 224-230 (2005).

[3] S. Dasgupta, J. Das, J. Eckert, I. Manna, J. Magn. Magn. Mater. **306**, 9-15 (2006).

[4] S.J. Park, Y.S. Song, K.S. Nam, S.Y. Chang, J. Kor. Powd. Met. Inst. **19**, 122-126 (2012).

[5] S.M. Hong, E.K. Park, K.Y. Kim, J.J. Park, M.K. Lee, C.K. Rhee, J.K. Lee, Y.S. Kwon, J. Kor. Powd. Met. Inst. **19**, 32-39 (2012).

[6] H.P. Klug, L.E. Alexander, Joohn Wiley and Sons, X-ray Diffraction Procedures for Polycrystalline and Amorphous Materials, New York 1997.

[7] L. Gao, H. Miyamoto, J. Inorg. Mater. **12**, 129-133 (1997).

[8] M. Tokita, J. Soc. Powder Technol. **30**, 790-804 (1993).

[9] T. Takeuchi, M. Tabuchi, H. Kageyama, Y. Suyama, J. Am. Ceram. Soc. **82**, 939-943 (1999).

[10] Z.J. Shen, M. Johnsson, Z. Zhao, M. Nygren, J. Am. Ceram. Soc. **85**, 1921-1927 (2002).

[11] G.D. Zhan, J.D. Kuntz, J.L. Wan, A.K. Mukherjee, Nat. Mat. **2**, 38-42 (2003).

[12] S.I. Cha, S.H. Hong, B.K. Kim, Mater. Sci. Eng. A **351**, 31-38 (2003).

[13] M. Yue, J.X. Zhang, Y.F. Xiao, G.P. Wang, T. Li, IEEE Trans. Magn. **39**, 3551-3553 (2003).

[14] S.Y. Chang, S.T. Oh, M.J. Suk, C.S. Hong, J. Kor. Powd. Met. Inst. **21**, 97-101 (2014).

[15] L. Zhao, H. Yang, L. Yu, Y. Cui, X. Zhao, B. Zou, S. Feng, J. Magn. Magn. Mater. **301**, 445-451 (2006).

[16] D.J. Kim et al., Korean Powder Metallurgy Inst, Powder Metallurgy & Particulate Materials Processing, Seoul 2010.